Survey of Space Born Night-time Light Sensing

Jakov Tutavac
Faculty of Electrical Engineering and Computing,
University of Zagreb, Croatia
contact: jakov.tutavac@fer.hr

***Abstract*—We have been accustomed to always-on night-time public illumination, without noticing that the light polluting emissions keep growing. Not only is the lighting infrastructure expanding, the technology of light is production is changing by employing white light-emitting diodes. To clarify the effects of this new lighting revolution, data which tracks the emitted light is needed. This article surveys the technology behind public lighting infrastructure, night-time remote sensing satellites, and the applications of the captured data. In addition, we list some of the challenges for observing the brightness of the Earth at night from space, and show an estimate of the faint light intensity using satellite observation data.**

***Keywords*—Remote sensing, spectroscopy, light emitting diodes, high intensity discharge lamps.**

I. Introduction

The number of light sources used for public illumination is increasing. There are two major concerns regarding the impact by excessive use of artificial public lighting. The first is increased light pollution, which is defined as the presence of artificial night-time light in the sky, estimated to have grown from 1992 to 2017 by at least 49% [1]. The second is increased energy usage, which negatively impacts the environment.

Not only is light pollution increasing, the light emission is changing in color from orange-green to spectrally broadband white light. As the complexity of public lighting architecture increases, new types of light sources replace conventionally used discharge lamps. Today, there is an on-going fourth lighting revolution [2], where high pressure sodium, high pressure mercury, and metal-halide lamps are being replaced with white light-emitting diodes (LEDs). White LEDs emit more blue light, when compared to discharge lamps, which has negative ramifications on the production of melatonin, a hormone that controls the sleep–wake cycle [3]. To research the effects of increased light pollution, night-time data as acquired by satellites from space observations is commonly used. However, this data does not include blue light emitted by LEDs. The focus of this work is surveying the technology behind capturing night-time light, mainly using space borne remote sensing.

The change in lighting architecture is one of the reasons methods and instruments for analyzing light pollution are an emerging technology. Presently, night-time data is publicly available on the internet from satellites such as the Suomi-NPP (VIIRS instrument), Luojia-1, and Jilin-1B. In the following sections, we overview lighting infrastructure, space born sensing, applications of night-time imaging, and two major challenges regarding night-time sensing. The challenges discussed include night-time light intensity and spatial, spectral and temporal resolution of the measurements.

II. Lighting infrastructure

This section overviews commonly used light sources for public lighting infrastructure. The discussion is presented in the following order: white LEDs, high-pressure sodium, high-pressure mercury, and metal-halide lamps. These light sources are used for public lighting due to their advantageous technical properties (energy efficacy and color rendition) and due to imposed governmental regulations on efficacy and light power emission. The light emission spectra, of each of the above-mentioned sources as measured by a spectrometer, are shown in Figure 1. The logarithmic plots are given in arbitrary intensity levels, and as such are only relatively intensity calibrated, but not absolutely. There are three major differences between the spectra of white LEDs and discharge lamps. White LEDs (i) emit broadband light, (ii) produce substantial blue light emission, and (iii) produce no emission in the wavelength regions above of red light. All of the three characteristics are due to the differences in the physical phenomena and technology behind the white LED, which is described in the following part.

A. White LEDs

Historically, solid state lighting was recently (in the previous decades) adopted as a public illumination light source. The most commonly adopted solid-state lighting device is the white light-emitting diode (LED), composed of a blue LED and a complimentary yellow phosphor. Figure 2 shows a cross-section photograph of a white LED. A thin layer of semiconductor, most commonly Gallium-Nitride based, that functions as the light emitting junction is grown on-top of a substrate. On top of the junction, a phosphor layer is deposited that may include a lens which collimates the emitted light. While the LED emits blue light, phosphor is used to convert the emitted light into white color. The required correlated-color temperature of the device is designed by the choice of phosphor and by the choice of LED.

Phosphor density and thickness are chosen to leak a predetermined fraction of the blue light emitted. The non-leaked fraction of blue light is mixed with the resulting

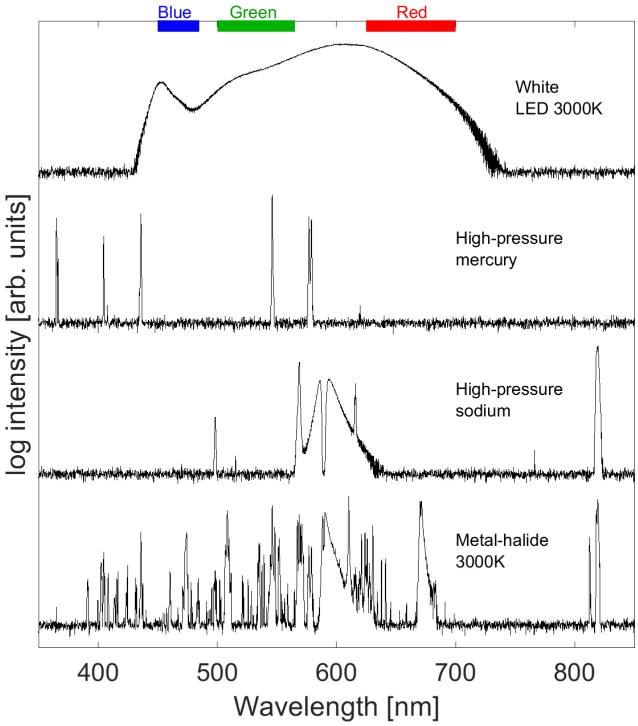

Figure 1: Logarithmic plot of the intensity spectra of white LED 3000K, high-pressure mercury, high-pressure sodium, and metal halide 3000K lamps.

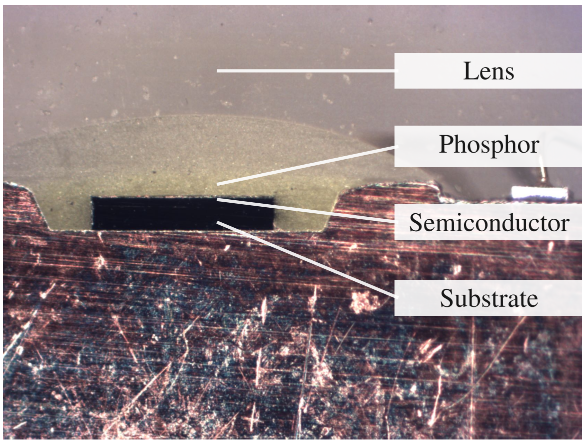

Figure 2: Cross-section of a white light-emitting diode.

yellow phosphor emission, which produces broadband white light. Striking the correct blue/yellow ratio depends upon having the correct amount, density, and particle size of phosphor, distributed evenly around the blue-emitting semiconductor [4].

The most commonly used phosphor is yttrium–aluminum garnets (YAG) doped with Ce^{3+} ions. The spectral properties of the phosphor allow for energy down-conversion of the peak LED emission at 460 nm into 520 nm and 580 nm bands. A blue AlInGaN LED, with a 465 central wavelength and 30-nm linewidth, allows for a feasible "white" LED with CCT ratings above 4000 K [5]. Low color temperatures (around 3000 K) cannot be attained using only YAG:Ce^{3+}-based

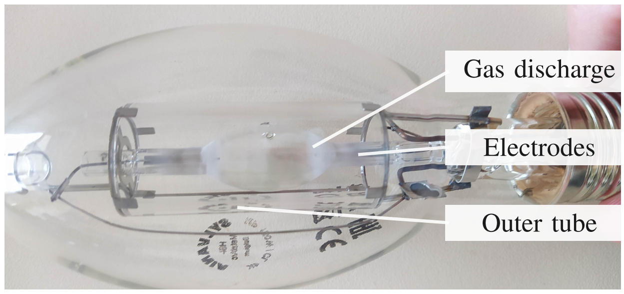

Figure 3: Photograph of a metal-halide discharge lamp.

phosphors, and require alternative phosphor families [6].

B. *Discharge lamps*

While solid state lighting is based on a semiconductor junction producing light, discharge lamps depend on plasma gas to radiate light. The light emitted by discharge lamps dramatically varies depending upon the plasma composition, or in other words, upon the constituent atomic elements. Therefore, the spectra of discharge lamps shown in Figure 1, consist of numerous spectral emission lines which emerge by spontaneous emission of photons from the plasma gas. The significant atomic elements contained within the plasma gas may include: sodium, mercury, and metals such as indium, thallium and lithium. The principal spectral emission lines are found in reference books or online [7], a part of which was used to construct Table I. The table lists spectral lines with ascending wavelength, denoting the atomic element and the light source(s) where the emission line is present. The light source types are denoted as HPS, HPM, and MH; which is short for high-pressure sodium, high-pressure mercury, and metal halide, respectively.

Discharge lamps, such as a metal halide lamp shown in Figure 3, consist of an inner tube filled with gas discharge, conductive electrodes, and an isolating outer tube for protection and light filtering. The gas atoms which are present in the inner tube determine the characteristics of the light, as well as the name (classification) of the discharge lamp. The following text describes some of the different classes of discharge lamps.

1) High-pressure sodium: The high-pressure sodium lamp is based on an electric discharge in sodium vapor where electrons, energized by the electric field, excite sodium atoms. The sodium vapor and a buffer gas such as xenon are contained within an arc tube of poly crstalline alumina. The arc tube with electrodes is mounted inside an outer bulb of fused silica.

The emitted light of the sodium lamp is yellow in color. The reason is that sodium has distinct spectral lines called D-lines at 588.9 nm and 589.5 nm. Depending on the pressure of the sodium vapor, the two spectral D-lines result in either emission lines or in absorption lines that are spectrally broadened.

An absorption line is formed when photons from a hot broad spectrum source pass through a cold material, such as an in homogeneous plasma of a high-pressure

Atomic element	Spectral line [nm]	Light sources presence
Hg	365.0	HPM, MH
Hg	404.7	HPM, MH
Hg	435.8	HPM, MH
In	450	MH
Na	497.8/498.3	HPS
Tl	534	MH
Hg	546.1	HPM, MH
Na	568.3/568.8	HPS
Hg	577.0	HPM, MH
Hg	579.1	HPM, MH
Na	589.0/589.6	MH
Li	610	MH
Na	615.4/616.1	HPS, MH
Li	670	MH
Na	818.4/819.5	HPS, MH

Table I: Spectral lines of atomic elements commonly present in discharge lamps for the wavelength region from 350 nm to 850 nm. Data taken from [7].

sodium lamp. High pressure increases self-absorption of the sodium D-lines and causes broadening effects, which redistributes the energy over a wide band of wavelengths.

The spectrum of the sodium lamp depends on plasma temperature distribution, sodium vapor pressure and discharge-tube diameter. The wavelength separation between the maxima of the self-reversed sodium D-lines depends approximately linearly on the sodium vapor pressure and is proportional to the square root of the discharge-tube radius [8]. The doublet emission lines of the high-pressure sodium lamp are: 497.8/498.3 nm, 568.3/568.8 nm, 615.4/616.1 nm, and 818.4/819.5 nm.

Detailed information about the high-pressure sodium lamp can be found in [8] and [9].

2) High-pressure mercury: The high pressure mercury discharge was investigated for the first time in 1906, by Küch and Retschinsky who published a paper on high-pressure mercury vapor discharges enclosed in evacuated quartz vessels [10].

The high-pressure mercury lamp is built with an outer glass like borosilicate, and an inner arc tube. The arc tube, made from fused silica, contains mercury and the starting gas argon.

A mercury discharge plasma has an approximately equal number of free electrons and ions. The maintenance of conductivity requires production of electron-ion pairs by recombination as fast as they are lost. In low-pressure discharge plasma, the principal recombination process is diffusion of electrons and ions to the tube wall and recombination there. The loss rate and required production rate are dependent on tube diameter and gas fill pressure [9].

An electric field accelerates the electrons, which causes inelastic collisions with mercury atoms which may excite them to upper energy states from which the atoms radiate. Around 65% of the electrical energy input could be radiated in a single line of the mercury spectrum, the 253.7 nm "resonance" line [9].

The UV 185.0 nm and 253.7 nm resonance lines form transitions which terminate on the ground state of the atom. By increasing pressure, the lines which result from transitions terminating in excited states instead of the ground state start to dominate. The UV resonance lines become relatively weak, and the VIS band lines radiate more strongly: 365.0, 404.7, 435.8, 546.1, 577.0, 579.1 nm.

The high pressure increases the rates of exciting collisions for all the states of the mercury atoms. The probability that a transition will take place can be expressed as the inverse of a lifetime. For the UV resonance lines, at high-pressure the lifetime becomes very long and accounts for their weakness in the emitted spectrum.

The overall energy efficiency of the high-pressure mercury lamp is 16% to 20% of the input power emitted as visible radiation, giving a total luminous efficacy of about 58 lm/W [9]. Mercury contains no emission lines with wavelengths above 579 nm in the visible band, causing poor appearance of objects illuminated by the mercury vapor lamp.

Detailed information about the high-pressure mercury lamp can be found in [9] and [10].

3) Metal-halide: Metal-halide arc lamps are a family of lamps which combine high luminous efficacy and good color rendition. The metal-halide arc lamp is built like the previously discussed mercury lamp: a quartz arc tube with two electrodes. The arc tube contains a rare gas for starting, and in operation, a high-pressure mercury vapor with the addition of various metal iodides. The idea of adding metal-halides dates back to 1911 [11], but it was not until the 1960s when metal iodide lamps were being commercially available [9].

The metal iodides become vaporized into the discharge and diffuse into the high-temperature arc where they dissociate. The now free metal atoms are excited by electron collisions and emit their own characteristic spectral lines. By then the metal atoms diffuse to the walls where they recombine with iodine atoms and form the iodide molecules once again.

Unlike pure metals which cannot be used, halides have a high enough vapor pressure and do not react with the silica tube. Around 50 metals can be satisfactorily used as iodide compounds. Since multiple metals can be used, a large number of combinations is possible. The choice of halides used is determined by the envisioned application of the lamp and the desired spectrum. The average excitation potential of the metals commonly employed is 4 eV or so as compared with 7.8 for mercury, and the total power radiated in the added metal spectrum can substantially exceed that of the mercury spectrum [9]. Many of the metals show a considerable number of emission lines in the VIS region, which is the main cause for the increased luminous efficacy of the metal-halide lamps when compared to the high-pressure mercury lamp.

Commonly used halides include indium, thallium, sodium, and lithium, which add shades of blue, green, yellow and red, respectively. The spectra of thorium, and scandium can be included and they consist of many emission lines spread all through the visible part of the spectrum. Plotted spectra of a wide variety of metal halide lamps can be found in [12]

III. Space born sensing and applications

In this section, we overview night-time imaging satellites which presently orbit the Earth at low orbit and capture publicly available data, in the following order: Suomi NPP (VIIRS), ISS, Luojia-1, and Jilin1-03B.

A. Suomi NPP (VIIRS)

The Earth at night composite image [13], which has become a popular poster, shows a global view compiled from over 400 night-time images which were captured by the Suomi National Polar-orbiting Partnership satellite that boards the VIIRS instrument. Today, the VIIRS instrument is the prime source of night-time data. This complex instrument weighting over 275 kg provides radiometrically calibrated images, with a night-time imaging accuracy shown to be within 15% [14] [15]. The design of the instrument is substantially sophisticated, consisting of two charge-coupled device arrays. The instrument allows for repeated measurements of a target, by employing time delay integration, to achieve a high signal-to-noise ratio. Each pixel of the resulting image has a ground spatial resolution of around 742×742 meters.

In [16], the authors examined VIIRS night-time imaging data of the San Meteo bridge located between San Francisco and San Jose, California. As the bridge is made of concrete and mostly illuminated at night, it is useful for analysis due to low background reflections of water. The results show that the radiance value of the VIIRS data is in agreement with the radiometrically predicted radiance value, with a relative error of 13%.

While it is calibrated, the most significant shortcoming of the VIIRS instrument is that the night-time data acquired only includes light with wavelengths between 500 nm to 900 nm. The resulting images are, therefore, monochromatic, and do not have separate spectral resolution channels. This is inadequate for future night-time Earth Observation missions because substantive portion of white LED emission is in the blue part of the spectrum (between 450 nm and 480 nm), and is not captured by the VIIRS instrument. It is neither possible to capture the 820 nm sodium spectral emission line, present in many discharge lamps, in a separate channel. In addition, VIIRS near-infrared imaging data is not available at night-time, to the author's best knowledge. As white LEDs are presently being installed for public illumination worldwide replacing discharge lamps, the additional blue light in the emission increases light pollution and presents a negative impact on wildlife and human life, due to its harmful effect on the circadian rhythm. Usage of VIIRS data for tracking these harmful effects is problematic due to the lack of blue light and near-infrared sensitivity.

B. International Space Station

Cities at Night is a citizen science project that aims to create a map, similar to Google maps, of the Earth at night using night-time color photographs taken by astronauts onboard the International Space Station (ISS). These photographs are publicly available data, containing over a million images taken at night. Nikon camera bodies and large aperture lenses are mainly used, where all of the cameras feature a Bayer filter which allows red, green and blue color imaging. While the low orbit of the ISS, at around 400 km, results in a high ground spatial resolution using professional grade cameras, there are several shortcomings of the imagery data.

First, we note that imaging the Earth at night with carefully selected frames, focus and exposure is difficult. Astronauts primarily work on station experiments and, as such, capturing photographs is only a secondary concern for them, which results in sporadically taken images of the Earth. Second, it would take extremely complex algorithms to interpret and catalog the photographs, hence the database is dependent on volunteers providing georeferencing.

Finally, problems with using ISS photographs for night-time studies include a lack of data processing and calibration, and the differences in the exact camera devices used. The ISS images require substantial processing and proper calibration to exploit intensities and ratios from the RGB channels. Although special tripods have been employed to partially compensate movement, some of the night-time images show movement incurred blurring. Some of the different possible calibration steps include: linearity correction, flat field/vignetting, astrometric calibration, georefercing, photometric calibration, atmospheric and window transmittance correction [17]. By applying these corrections it is possible to analyze ISS images and to estimate spatial and temporal variation in the spectrum of artificial light emissions [18].

C. Commercial satellites

Other state of the art sources of night-time data include commercial satellites equipped with (red, green and blue channel) cameras: Jilin1-03B (sensitive from 430 – 720 nm) and Luojia 1-01 (sensitive to light from 480 nm to 800 nm). Although their imaging payloads feature a large spatial resolution, their main shortcoming is the lack of a separate spectral channel sensitive to near-infrared light which would capture the doublet-820 nm sodium spectral emission line.

The Luojia-1 satellite [19] [20] [21] was launched on June 2, 2018. It was developed by the Wuhan University with the goal of capturing high-resolution night-time images. Luojia-1 is on a polar orbit at an altitude of 645 km. The remote sensing instruments on-board the satellite feature: a high spatial resolution of 130 m, 8-bit image data, and on-board radiance calibration.

The Jilin1-03B satellite [22] [23] was launched on January 9, 2017 by the Chinese commercial satellite company: Chang Guang Satellite Technology Co., Ltd., and began commercial operation on April 1, 2017 (http://www.charmingglobe.com). Jilin1-03B is on a sun-synchronous orbit at an altitude of 535 km. The remote sensing instruments on-board the satellite feature: a very high spatial resolution of 0.92 m, 8-bit image data, and on-board radiance calibration. The light is captured in three different color bands: blue (430 - 512 nm), green (489 - 585 nm), and red (580 - 720 nm).

D. Applications of night-time imaging

Although night-time Earth imaging is a niche market, it has a potential for a number of commercial applications, some of which are discussed here with references provided. However, future trends of night-time imaging are not discussed.

Since the industrial Era, there has been an increase in urbanization, the large population migration from rural areas to urban areas. Tracking urbanization is possible using night-time imaging data. Cities are brightly lit during the night, unlike rural areas which are lacking in lighting infrastructure. Therefore, it is possible to quantify the brightness of cities and compare it to the brightness of rural areas. When high spatial resolution night-time imaging is used, the border separating urban and rural areas is easily noticeable by the change in light brightness. It has been shown that the increase in light intensity correlates with the increase in population in cities [20].

An important application of night-time light data is found in econometrics, where correlations with the Gross Domestic Product are used to estimate wealth and regional economic phenomena such as inequality and poverty [24]. Comparison of annual average light data for 2014–2016, and metropolitan statistical area data published by the U.S. Office of Management and Budget, resulted with positive correlations. Therefore, VIIRS data was shown useful to estimate cross-sectional Gross Domestic Product values [25]. In addition, 2012 VIIRS night-time light composite data used to estimate county-level poverty in China, was shown to correlate with socioeconomic statistics. Estimation of regional poverty level is precondition for the government and policy makers to reduce poverty in China, for which VIIRS data shows to be a promising alternative data source [26] [27].

Light imagery data from the Jilin1-03B satellite was used for monitoring the spatial pattern and discriminating the types of artificial light in Hangzhou, China. By using a machine learning based method (C4.5 decision tree classifier) two light sources types were classified: the high-pressure sodium lamp and white LEDs, by incorporating their spectral information and morphology feature. The results showed an overall accuracy of 84% for separating light emitted by sodium lamps and white LEDs [22]. Once the sodium lamps are identified it is possible to simulate replacing them by solar street lights, as to estimate the amount of electrical energy saved [23].

Other examples of applications include: natural gas flaring detection [28], quantify the extent of light outage and its recovery during and after storms [29], and correlating the night-time light of a country and its total carbon dioxide (CO2) emissions [30].

IV. Challenges

A. Light intensity

The main challenge in capturing night-time light from Space is the faint light intensity which reaches the detector. Therefore, it is necessary to precisely define the level of light intensity. Namely, in this section we show two estimates of night-time data using data as acquired by the before-mentioned VIIRS instrument.

In general, when given a radiant flux (light energy considered per unit time) that impinges a lens with area A_{lens}, the *irradiance* per lens area measured in W/m^2 is:

$$E = \frac{\Phi}{A_{lens}}. \tag{1}$$

In this section, we show that the estimate of the night-time irradiance, when overlooking the City of Zagreb with a 200 km diameter, is approximately $1.3\,\mathrm{pW/mm^2}$.

The radiant flux as seen by a detector overlooking a source region S is given with the surface integral:

$$\Phi = \iint_S L\,\cos(\theta)\;\Omega\,\mathrm{d}A \tag{2}$$

where L is the radiance of the source, $\mathrm{d}A$ is the infinitesimal area of the source and Ω is the solid angle subtended by the detector from the point of view of the source.

To find the irradiance (in W/m^2) given in Eq. (1), the surface integral in Eq. (2) must be solved. If the radiance L is assumed to be uniform over the source region S, the solution can be analytically expressed. Since public lighting infrastructure is concentrated in urban centers and lacking in rural areas, nighttime radiance is highly non-uniform. This is the reason an in-house program was written which numerically solved this integral. Results for both the analytical expression and numerical method are given. The mathematical derivation of both methods follows.

1) Analytical expression: We assume the lambertian source with radiance $L(\theta) = L\cos\theta$ is a circular disk of finite radius R. This source is observed at a point positioned orthogonal to the center of the disk at distance h. The differential area is projected with respect to the angle θ between the normal of the differential surface and the direction of the observation point $\mathrm{dA}\,\cos\theta$. The same angle increases the distance on which the solid angle depends:

$$\Omega = \frac{A_{lens}}{h^2\,\cos^{-2}\theta} \tag{3}$$

Therefore, the surface integral for radiant flux (from Eq. 2) can be simplified as:

$$\Phi_1 = \iint L\cos\theta\,\frac{\cos^2\theta}{h^2}\,\cos\theta\,A_{lens}\,\mathrm{d}A \tag{4}$$

For an uniform radiance L, which does not depend on the differential surface area $\mathrm{d}A$, the radiance can be left out of the integral:

$$\Phi_1 = \frac{A_{lens}L}{h^2}\int_0^R\int_0^{2\pi}\cos^4(\theta(r))\,r\,\mathrm{d}\varphi\,\mathrm{d}r \tag{5}$$

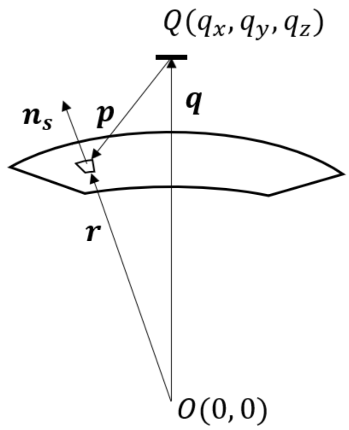

Figure 4: Earth surface area as viewed from an imaging instrument on a satellite located at point Q.

where polar coordinates were used:

$$r = h\ \tan\theta \tag{6}$$

$$dr = \frac{h}{\cos^2\theta}\,\mathrm{d}\theta \tag{7}$$

The integral is simplified with $\tan\theta = \sin\theta\,/\,\cos\theta$ into the following expression

$$\Phi_1 = 2\pi A_{lens} L \int_0^{\theta_{max}} \cos\theta\ \sin\theta\ \mathrm{d}\theta \tag{8}$$

The solution for the radiant flux is:

$$\Phi_1 = \pi A_{lens} L \sin^2\theta_{max} \tag{9}$$

where $\theta_{max} = \arctan\left(R\,/\,h\right)$.

Finally, the irradiance is:

$$E_1 = \pi L \sin^2\theta_{max} \tag{10}$$

2) Non-uniform radiance: The equation of a spheroid centered at the origin is given in Cartesian coordinates by:

$$\varphi\left(x,y,z\right) = \frac{x^2+y^2}{R_a^2} + \frac{z^2}{R_b^2} = 1 \tag{11}$$

where R_a is the semi-major axis and R_b is the semi-minor axis (polar radius of the Earth). Both R_a and R_b are given for the reference ellipsoid used to model the Earth. ($R_a =$ 6378.1370 km and $R_b = 6356.7523$ km.)

The normal vector at point (x, y, z) of the surface of the spheroid is:

$$\begin{aligned}\mathbf{n_s} &= \nabla\varphi\left(x,y,z\right) = \\ &= \frac{2x}{R_a^2}\,\mathbf{i} + \frac{2y}{R_a^2}\,\mathbf{j} + \frac{2z}{R_b^2}\,\mathbf{k}\end{aligned}$$

The surface of a spheroid in the region $S \subseteq \mathrm{R}^3$ can be parameterized with (u, v) as a surface in region $A \subseteq \mathrm{R}^2$ as:

$$\mathbf{r}\left(u,v\right) = x(u,v)\mathbf{i} + y(u,v)\mathbf{j} + z(u,v)\mathbf{k} \tag{12}$$

where u and v are commonly expressed as latitude and longitude, respectively.

A scalar field is a function which associates a scalar value for every point in space, such as radiance data:

$$L\left(x,y,z\right) = L\ \cos^2\theta\ \cos\gamma \tag{13}$$

The function is evaluated over a surface integral in Cartesian coordinates:

$$\Phi_3 = \iint_S L\left(x,y,z\right)\ \Omega\,\mathrm{d}S \tag{14}$$

The solid angle Ω depends on the distance of the differential source area and the point of observation Q described with the radial vector $\mathbf{q}$:

$$\Omega = \frac{A_{lens}}{\|\mathbf{p}\|^2} \tag{15}$$

$$\mathbf{p} = \mathbf{r} - \mathbf{q} \tag{16}$$

$$\cos\theta = \frac{(\mathbf{n_s}|\mathbf{p})}{\|\mathbf{n_s}\|\|\mathbf{p}\|} \tag{17}$$

$$\cos\gamma = \frac{(\mathbf{n_d}|\mathbf{p})}{\|\mathbf{n_d}\|\|\mathbf{p}\|} \tag{18}$$

Finally, the irradiance is:

$$E_3 = \frac{1}{A_{lens}} \iint_S L\,\Omega\ \cos^2\theta\ \cos\gamma\,\mathrm{d}S \tag{19}$$

complex analytically since L is not uniform

observes the Earth at satellite zenith angles ranging from zero (nadir) to 70 degrees (edge of scan).

3) Data: Nighttime radiance data used was taken by the Suomi National Polar-orbiting Partnership Satellite launched in October 2011. The key instrument payload is the Visible Infrared Imaging Radiometer Suite (VIIRS). Out of the twenty-two spectral bands (channels) available in the VIIRS instrument, the day-and-night band (DNB) with a spectral range from 500 - 900 nm is used to composite nighttime radiance data. The ground image resolution is approximately 720 meters.

The nighttime radiance data, taken between dates 1/1/2019 - 31/12/2019, was downloaded from the site lightpollutionmap [31]. The two dimensional floating point data corresponds to each pixel of the VIIRS DNB is in a GeoTIFF file format. The corner pixels reference locations on Earth with latitude and longitude as defined by World Geodetic System 1984 (WGS 84), a geodetic coordinate system. The WGS 84 [32] defines an ellipsoid as given in Equation (11) with the semi-major axis $R_a = 6378.1370$ km and semi-minor axis $R_b = 6356.7523$ km.

MATLAB script to load the GeoTIFF file format iterate through the matrix pixel data and using Equation 19

4) Results: Night-time VIIRS radiance data was used to estimate the night-time irradiance reaching an optical-imaging system lens. The lens is assumed to be positioned above the source at a distance of 500 km. Table II contains the estimated irradiance values. E_1 is the estimated value by the analytical expression, while E_2 is the estimated value by the numerical analysis. The results show that there are negligible differences in the results of both methods. Therefore, for night-time light estimation it is sufficient to use the approximated analytical expression.

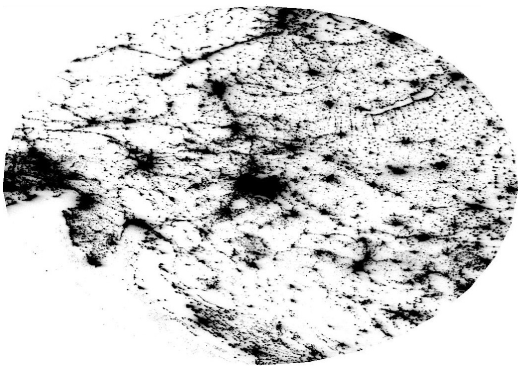

Figure 5: VIIRS yearly nighttime radiance, Croatia (Zagreb). FOV diameter 500 km.

FOV dia [km]	100	200	500
E_1 [pW/mm^2]	0.783	1.284	4.137
E_2 [pW/mm^2]	0.788	1.306	4.045

Table II: Estimated night-time irradiance, calculated using data from the VIIRS DNB (500 - 900 nm).

B. Resolution

Low Earth Orbit night-time imaging has two major challenges. While the first one is the low light intensity described previously, the second one is related to resolution and can be split into three parts: temporal, spatial, and spectral resolution.

Temporal resolution is primarily dependent on the satellite orbit, and not on the design of the electro-optical measurement system. None of the satellites discussed previously (Suomi-NPP, Luojia, Jilin1-03B, ISS) are geostationary, which would allow for night-time imaging of the entire hemisphere, but are rather bodies located in a low Earth orbit. This results in measurements with infrequent revisits of a desired location, and hence poor temporal resolution across the night.

Unlike temporal resolution, spatial and spectral depend on the design of the electro-optical system. Typically, light measurement systems consist of an optical lens and a detector. The glass used for lens fabrication affects its light transmission properties, weight and cost. For example, quartz and fused silica allow for UV imaging due to UV light transparency. This is one of the reasons these more expensive glasses are preferred to less expensive borosilicate glass or acryilic plastic. Another reason is solarization, the process of deterioration in light transmission due to high energy photons or particles, to which quartz and fused silica are less susceptible, when compared to borosilicate glass [33]. Since the light intensity is feeble, satellite optics commonly feature large diameter lenses that are high-cost and heavy, and are generally prohibitive for small CubeSats. The lens may be incorporated into the housing of the detector, fabricated directly on top of the active area, or omitted. While lens integration may save weight and volume, such devices are even higher in costs and ultimately overly expensive for small volume designs, such as non-constellation CubeSats. Therefore, cconsumer-of-the shelf components for detectors, lenses, and image sensors are preferred and limit the creativity in design of the electro-optical system.

In-between the lens and the detector, an optical filter may be used. The filter characteristic can be short-pass, long-pass, band-pass or band reject. Multiple filters can be used with any of the above-mentioned filtering characteristics. In addition, the filter can be integrated on-top of the active area of the individual pixels of the detector. Most commonly used are infrared filters, added between the camera and the lens. The choice of optical filtering depends on the application of the night-time imaging data. While optical filtering may customize the spectral resolution of the instrument, it reduces the number of photons reaching the active area of the detector, thereby lowering the signal-to-noise ration. This is problematic for night-time imaging as the signal-to-noise ratio is low to begin with. Therefore, either monochromatic imaging (VIIRS DNB) or red, green and blue imaging (Luojia, Jilin1-03B, ISS) are currently used for space born night-time sensing. This shows that at the time of writing, custom spectral resolution night-time data is not available, and may prove to be a future possibility.

Detectors convert the light into a current which is amplified and measured by further electronics. Detectors can be a semiconductor device, phototube or some other kind of light converting device. For semiconductor devices, the process of conversion depends on the fabrication process, the multiple-step sequence of photolithographic and chemical processing steps during which electronic circuits are gradually created on a wafer made of pure semiconducting material. Typically, silicon and indium gallium arsenide is used, but others such as gallium arsenide or silicon carbide can be used. The responsivity of the detector, which describes the efficacy of conversion from light to current, is highly wavelength dependent and differs depending on the type of semiconductor used. Typically, a transimpedance amplifier or a time-variable integrator circuit is used to convert the photocurrent into a voltage which is digitized by an analog-to-digital converter. The electronic operating circuits for signal conditioning and digitization can be integrated in the detector or designed externally. Depending on the spatial resolution, detectors are divided into: single pixel, linear array, or area sensors. All of the satellites discussed in this work feature area imaging sensors with a high pixel density. While higher spatial resolution resulting with more detailed photographs of the Earth may seem desireable at first, there is a trade-off regarding spatial resolution and dynamic range.

V. Conclusion

The world is in the midst of a new "lighting revolution" due to the development of light emitting diode technology, which is altering the night-time emission from the surface of the Earth that can be measured from space. There are many challenges associated with remote sensing of this emission. The most prominent of these are the light intensity and the large required dynamic range of night scenes, when compared to daytime remote sensing. In addition, careful planning of the electro-optical system is needed such that the data meets the desired application, regarding: spectral, spatial and temporal resolution. Currently, nighttime imaging data is available from several sources, where each has its own advantages and disadvantages. However, new and improved sensors and methods may introduce novel remote sensing applications and result in the change in our understanding of light pollution and its effects.

REFERENCES

[1] Sánchez de Miguel, Alejandro, et al. *"First Estimation of Global Trends in Nocturnal Power Emissions Reveals Acceleration of Light Pollution."* Remote Sensing 13.16 (2021): 3311.

[2] Pust, P., Schmidt, P. J., and Schnick, W. *"A revolution in lighting."* Nature materials 14.5 (2015): 454-458.

[3] Lamphar H. A. S., and Kocifaj M. *"Light Pollution in Ultraviolet and Visible Spectrum: Effect on Different Visual Perceptions."* PLoS ONE 8(2): e56563. 2013. doi:10.1371/journal.pone.0056563

[4] Steigerwald, Daniel A., et al. *"Illumination with solid state lighting technology."* IEEE journal of selected topics in quantum electronics 8.2 (2002): 310-320.

[5] Shur, Michael S., and R. Zukauskas. *"Introduction to solid-state lighting."* Wiley-Interscience. 1-st edition, 2002.

[6] Shur, Michael S., and R. Zukauskas. *"Solid-state lighting: toward superior illumination."* Proceedings of the IEEE 93.10 (2005): 1691-1703.

[7] Handbook of Basic Atomic Spectroscopic Data. NIST Standard Reference Database 108. 2013. doi:10.18434/T4FW23

[8] de Groot, Josephus Johannes, and J. A. J. M. Van Vliet. *"The high-pressure sodium lamp."* Macmillan International Higher Education, 1986.

[9] Waymouth, John F. *"Electrical discharge lamps."* Cambridge, MA: MIT Press, 1971.

[10] Elenbaas, Willem, et al. *"High Pressure Mercury Vapour Lamps and Their Applications."* NV Philips Gloeilampenfabrieken, 1965.

[11] Steinmetz, Charles P. *"Electric lighting."* U.S. Patent No.: 1006021. 17 Oct. 1911.

[12] Reiling G. H. *"Characteristics of Mercury Vapor–Metallic Iodide Arc Lamps."* JOSA 54.4: 532-540, 1964.

[13] NASA Earth Observatory image using Suomi NPP VIIRS data. 2009. https://www.nasa.gov/topics/earth/earthday/gall_earth_night.html

[14] Liao, L.; Weiss, S.; Mills, S.; Hauss, B. *"Suomi NPP VIIRS day-night band on-orbit performance."* J. Geophys. Res. 2013, 118, 12705–12718.

[15] Cao, C., et all. *"Suomi NPP VIIRS sensor data record verification, validation, and long-term performance monitoring."* J. Geophys. Res. 2013, doi:10.1002/2013JD020418.

[16] Cao C, Bai Y. *Quantitative Analysis of VIIRS DNB Nightlight Point Source for Light Power Estimation and Stability Monitoring.* Remote Sensing. 2014; 6(12):11915-11935. https://doi.org/10.3390/rs61211915

[17] Sánchezde Miguel, Alejandro, et al. *"Colour remote sensing of the impact of artificial light at night (II): Calibration of DSLR-based images from the International Space Station."* Remote Sensing of Environment 264 (2021): 112611.

[18] Sánchez de Miguel, Alejandro, et al. *"Colour remote sensing of the impact of artificial light at night (I): The potential of the International Space Station and other DSLR-based platforms."* Remote sensing of environment 224 (2019): 92-103.

[19] Jiang W., et al. *"Potentiality of using Luojia 1-01 nighttime light imagery to investigate artificial light pollution."* Sensors 18.9 (2018): 2900.

[20] Zhai W., Han B., and Cheng C. *"Evaluation of Luojia 1–01 nighttime light imagery for built-up urban area extraction: A case study of 16 cities in China."* IEEE Geoscience and Remote Sensing Letters 17.10 (2019): 1802-1806.

[21] Feng G., et al. *"How to account for endmember variability in spectral mixture analysis of night-time light imagery?."* International Journal of Remote Sensing 41.8 (2020): 3147-3161.

[22] Zheng, Qiming, et al. *"A new source of multi-spectral high spatial resolution night-time light imagery—JL1-3B."* Remote sensing of environment 215 (2018): 300-312.

[23] Cheng B., et al. *"Automated extraction of street lights from JL1-3B nighttime light data and assessment of their solar energy potential."* IEEE Journal of Selected Topics in Applied Earth Observations and Remote Sensing 13 (2020): 675-684.

[24] Prakash A., Shukla A. K., Bhowmick C., and Beyer R. C. M. *"Night-time Luminosity: Does it Brighten Understanding of Economic Activity in India?"* Reserve Bank of India Occasional Papers, Vol. 40, No. 1, 2019.

[25] Chen X., and Nordhaus W. D. *"VIIRS nighttime lights in the estimation of cross-sectional and time-series GDP."* Remote Sensing 11.9 (2019): 1057.

[26] B. Yu, K. Shi, Y. Hu, C. Huang, Z. Chen and J. Wu, *"Poverty Evaluation Using NPP-VIIRS Nighttime Light Composite Data at the County Level in China."* IEEE Journal of Selected Topics in Applied Earth Observations and Remote Sensing, vol. 8, no. 3, pp. 1217-1229, March 2015, doi:10.1109/JSTARS.2015.2399416.

[27] Li X., et al. *"Potential of NPP-VIIRS nighttime light imagery for modeling the regional economy of China."* Remote Sensing 5.6 (2013): 3057-3081.

[28] Elvidge C. D., Zhizhin M., Baugh K., Hsu F.C., and Ghosh T. *"Methods for global survey of natural gas flaring from visible infrared imaging radiometer suite data."* Energies 9 (1), 14. 2015.

[29] C. Cao, X. Shao and S. Uprety, *"Detecting Light Outages After Severe Storms Using the S-NPP/VIIRS Day/Night Band Radiances."* IEEE Geoscience and Remote Sensing Letters, vol. 10, no. 6, pp. 1582-1586, Nov. 2013, doi:10.1109/LGRS.2013.2262258.

[30] Ou J., Liu X., Li X., Li M., and Li W. *"Evaluation of NPP-VIIRS nighttime light data for mapping global fossil fuel combustion CO2 emissions: a comparison with DMSP-OLS nighttime light data."* PLoS One 10 (9), e0138310. 2015.

[31] Jurij Stare, "www.lightpollutionmap.info". VIIRS 2019 data, "Earth Observation Group, NOAA National Geophysical Data Center".

[32] "World geodetic system 1984", Department of defense, National Geospatial-Intelligence Agency (NGA) standardization document, 2014.

[33] Bach, H., and Neuroth N. *"The properties of optical glass."* Springer Science and Business Media. 1998.